

Final Draft
of the original manuscript:

Wang, L.; Razzaq, M.Y.; Rudolph, T.; Heuchel, M.; Noechel, U.; Mansfeld, U.;
Jiang, Y.; Gould, O.E.C.; Behl, M.; Kratz, K.; Lendlein, A.:

**Reprogrammable, magnetically controlled polymeric nanocomposite
actuators.**

In: Materials Horizons. Vol. 5 (2018) 5, 861 - 867.

First published online by Royal Society of Chemistry: 21.06.2018

<https://dx.doi.org/10.1039/C8MH00266E>

Reprogrammable, Magnetically Controlled Polymeric Nanocomposite Actuators

Li Wang^{a,b,#}, Muhammad Yasar Razzaq^{a,#}, Tobias Rudolph^a, Matthias Heuchel^a, Ulrich Nöchel^a, Ulrich Mansfeld^a, Yi Jiang^{a,b}, Oliver E. C. Gould^a, Marc Behl^a, Karl Kratz^a, Andreas Lendlein^{a,b}*

^aInstitute of Biomaterial Science, Helmholtz-Zentrum Geesthacht, Kantstr. 55, 14513 Teltow, Germany

^bInstitute of Chemistry, University of Potsdam, Karl-Liebknecht-Str. 24-25, 14476 Potsdam, Germany

[#] authors contributed equally

*corresponding author: andreas.lendlein@hzg.de

Keywords: soft actuator, nanocomposite, remote control, alternating magnetic field, iron oxide nanoparticles

Soft robots and devices with the advanced capability to perform adaptive motions similar to that of human beings often have stimuli-sensitive polymeric materials as the key actuating component. The external signals triggering the smart polymers' actuations can be transmitted either via a direct physical connection between actuator and controlling unit (tethered) or remotely without a connecting wire. However, the vast majority of such polymeric actuator materials are limited to one specific type of motion as their geometrical information is chemically fixed. Here, we present magnetically driven nanocomposite actuators, which can be reversibly reprogrammed to different actuation geometries by a solely physical procedure. Our approach is based on nanocomposite materials comprising spatially segregated crystallizable actuation and geometry determining units. Upon exposure to a specific magnetic field strength the actuators' geometric memory is erased by the melting of the geometry determining units allowing the implementation of a new actuator shape. The actuation performance of the nanocomposites can be tuned and the technical significance was demonstrated in a multi-cyclic experiment with several hundreds of repetitive free-standing shape shifts without losing performance.

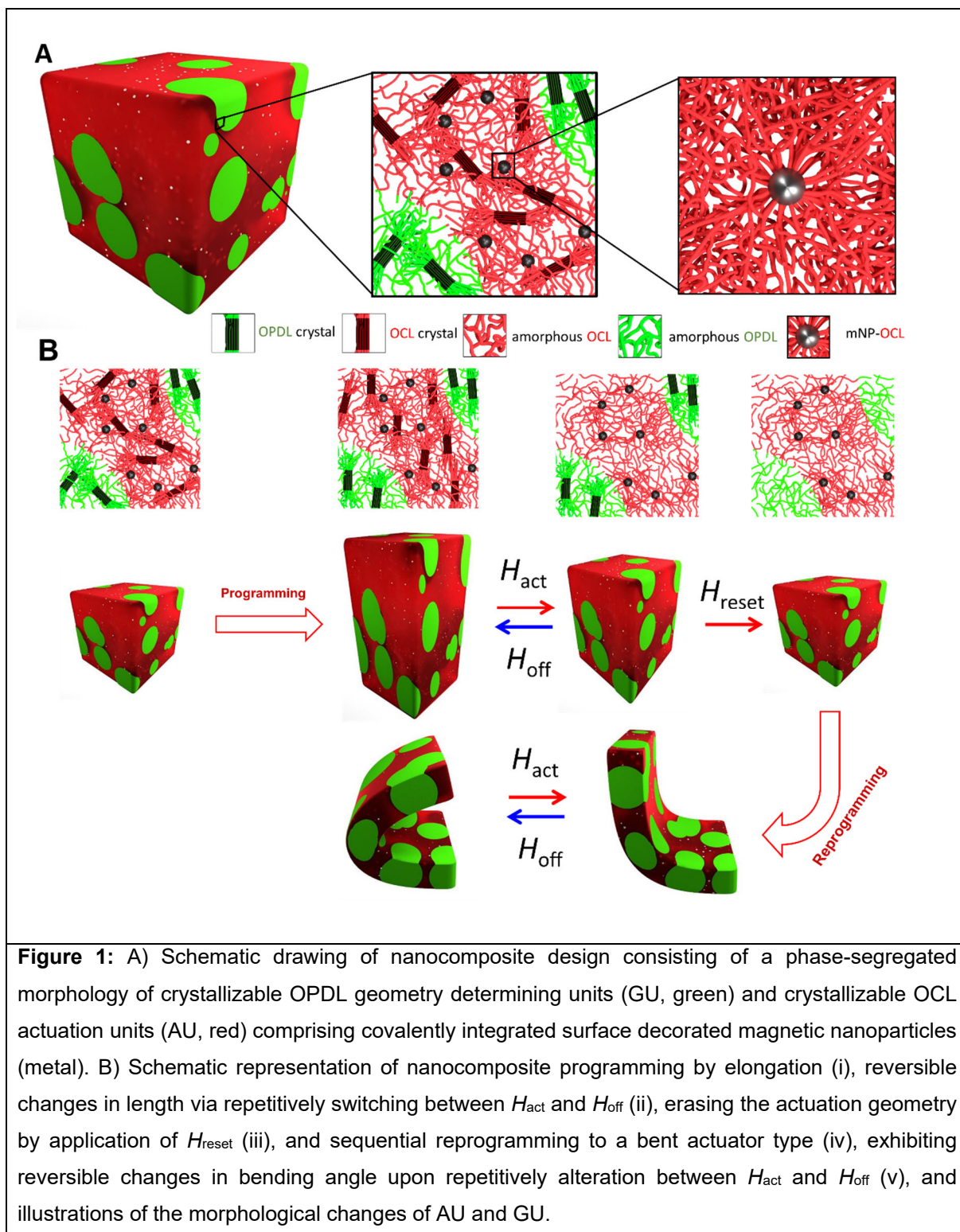
Soft actuator materials based on stimuli-sensitive polymers or composites with specific chemical compositions and architectures have inspired modern applications including robotics, artificial muscles, and energy harvesting materials or production technologies.¹⁻⁴ Here, the reversible actuation depends on the sensitivity to an external stimulus e.g., heat, light, humidity or electricity.⁵⁻⁷ The desired actuation of these materials is triggered via signals of a controlling unit, which is either tethered (physically connected) or in direct contact with the actuator or can remotely (untethered) control the motions. Some examples of tethered soft actuators are fluid-powered, fibre-reinforced elastomeric devices⁸ or electro-active polymers requiring direct contact of the electrodes with the actuator.^{6,9-11} Untethered systems have been realized by cyclic thermal expansion and contraction in twisted polyamide and polyethylene monofilaments upon repetitive heating and cooling, resulting in high stress actuations (while a constant stress is applied to the system).¹² In contrast, free-standing reversible bidirectional shape-shifts in crystallizable crosslinked polymer networks under similar cyclic conditions are based on conformational changes of the oriented actuation units (AU) undergoing melt-induced contraction (MIC) and crystallization-induced elongation (CIE) on different length scales.^{13, 14} Other examples include photomechanical polymer systems based on liquid-crystalline elastomers (LCE), which can be remotely actuated by visible light,¹⁵ while irradiation with infrared light controls the motions in LCE / carbon nanotube composites¹⁶. Near infrared light triggered photoactuation was achieved in reconfigurable monodomain liquid crystalline vitrimer composites containing organic polydopamine nanoparticles¹⁷. Recently, static and alternating magnetic fields have emerged as the most prominent non-contact and non-invasive trigger for soft actuator materials, because of their large penetration range for various environmental conditions. In this context, micro-pump systems prepared from multi-material laminates¹⁸ or composites with magnetic particles¹⁹ as well as soft deployable structures²⁰ have been reported. Reversible deformations in magneto-responsive polymer composites can be achieved by orienting or directing the magnetic fillers and thereby the flexible material (i.e.

elastomers, hydrogels or LCEs) itself.²¹⁻²⁶ In addition to these classical approaches, where the actuator shape is directly manipulated by the applied magnetic field, single reversible shape changes can be obtained for LCE composites containing magnetic iron oxide nanoparticles by inductive heating in alternating magnetic fields (AMF).²⁷ The parameters, which control the inductive heating of polymeric composites in AMF are: the nature of mNPs (i.e. the intrinsic loss power), the mNP concentration and their dispersion profile as well as the material's design (i.e. surface area-to-volume ratio), which can critically affect heat transport and in this way the actuation.²⁸⁻³¹ LCE composite materials have predefined actuation shapes with permanently chemically integrated geometrical information, and enable only one single motion. This limitation motivated our research on reprogrammable, magnetically controlled polymeric nanocomposite reversible actuators. Providing a magnetic field, independent actuator shapes can be programmed by physical manipulation and thus allow an almost arbitrary alteration of the actuators' geometry and motion. The magnetically-induced reversible motion of the actuator is achieved by applying a suitable actuation magnetic field strength (H_{act}) and switching off the magnetic field (H_{off}). Exposing the programmed actuator to $H_{\text{reset}} > H_{\text{act}}$ erases the actuation geometry so that a new actuator motion can be programmed (encoded) afterwards.

Our strategy to realize such a magnetic composite material involves the synthesis of a multiphase polymer network nanocomposite with a distinct heterogeneous morphology of crystallizable actuation (AU) and geometry-stabilizing units (GU) along with covalently integrated magnetic nanoparticles (mNPs) as schematically displayed in [Figure 1A](#). The AU volume fraction in the nanocomposite was designed as continuous phase and its content should be as high as possible to enable pronounced reversible actuations. The thermomechanical more stable GU ($T_{\text{m,AU}} < T_{\text{m,GU}}$) were distributed homogeneously throughout the actuator to provide the overall stability during actuation and magneto- or thermomechanical programming processes defining the actuator shape. The magneto-sensitive nanosensors should be homogeneously dispersed in the nanocomposite to enable efficient indirect heating. The

actuation principle of the presented nanocomposites relies on the melting induced contraction of the AU upon inductive heating in the AMF and oriented crystallization of the actuation segments when the AMF is switched off. One specific feature of the presented materials is that their actuation geometry can be programmed by solely physical processes (i.e. magneto- or thermomechanical procedures), whereby the programming is completely reversible and can be altered almost arbitrarily. Here, melting and re-establishment of the GU allows to reprogram the nanocomposite in any actuation geometry.

The challenge for the fabrication of such a remote-controlled actuator was addressed by a polymer network nanocomposite with hierarchical organization on the micro- and nano-scale. For the synthesis of multiphase nanocomposites, star-shaped oligomeric ϵ -caprolactone (stOCL) precursors, serving as crystallizable AU ($T_m \sim 50$ °C; SI Table S2), star-shaped oligomeric ω -pentadecalactone (stOPDL) precursors ($T_m \sim 83$ °C; SI Table S2), functioning as GUs, and oligomer decorated magnetic iron oxide nanoparticles (mNP-OCL or mNP-OPDL) were reacted in the presence of hexamethylene diisocyanate (HDI) as a linker ([for details see SI 1.1 Experimental](#)). A schematic illustration of the nanocomposites' structural elements (AU, GU, and mNP) is given in [Figure 1 A](#).



Details about the basic nanocomposite characteristics i.e. composition, thermal and mechanical properties, phase-segregated morphology of AU and GU, and dispersion of the mNPs in the material are provided in [SI 1.2 Nanocomposite Characteristics](#). Importantly the composites display well-separated melting temperatures (T_m) for OCL and OPDL, of ~ 50 °C and ~ 80 °C,

which were determined by differential scanning calorimetry (DSC). These values define the temperature ranges, in which the thermal transitions allow us to perform actuation (T_{act}) and reprogramming (T_{reset}) of the nanocomposites. Here, OCL was specifically selected as AU with relatively slow crystallization kinetics, which allows to nicely control the actuation behavior by the variation of the cooling rate³². Investigations by electron microscopy and atomic force microscopy indicate a phase-segregated morphology of the organic part with GU droplets of 1 to 5 μm in the AU dominated matrix (see SI Figures S2 and S4). Composites with homogeneously dispersed nanoscale magnetic sensors were achieved when the synthesis was performed with OCL decorated mNPs, while utilizing a mixture of OPDL and OCL modified mNPs resulted in an inhomogeneous dispersion of the nanoparticles accumulating at the AU/GU interphase (see SI Figure S2). Inductive heating experiments in an AMF at $H_{\text{high}} = 12.1 \text{ kA}\cdot\text{m}^{-1}$ revealed a higher achievable temperature of $60 \pm 1 \text{ }^\circ\text{C}$ for the composite with OCL decorated nanoparticles, while only $50 \pm 1 \text{ }^\circ\text{C}$ were achieved for the composite prepared with the nanoparticle mixture (see SI section 3.2 Magnetic Heating Behavior and Figure S6A). At a temperature of $50 \pm 1 \text{ }^\circ\text{C}$ the OCL AU are not completely molten and some OCL crystals are still existent. We attribute the lower magnetic heating efficiency of the nanocomposite comprising both types of nanoparticles to the inhomogeneous dispersion of the magnetic sensors.

In a set of preliminary experiments the thermally-initiated actuation function (no magnetic field presence) was explored for nanocomposites with identical mNP content but different AU to GU ratios. Cyclic, uniaxial thermomechanical tensile tests as well as temperature-dependent AFM and in-situ X-ray scattering experiments were applied for quantifying the actuation function on different length scales (see SI 2.1 Experimental and 2.2 Thermal Actuation Behavior). Here, the best actuation performance, with reversible macroscopic length changes of approximately 5%, was obtained for the nanocomposite with an AU to GU ratio of 85/15 (wt/wt) and homogeneously dispersed OCL decorated magnetic nano-sensors, which were selected for

further remote actuation experiments. The thermally-induced actuation performance of this composite actuator was similar to that obtained for multiphase copolymer networks prepared from the identical oligomeric precursors (without inorganic nanoparticles), which exhibited a reversible strain of $\varepsilon_{\text{rev}} \sim 6\%$. Interestingly, for the same compositional material (85/15 wt%) and the mNP-OCL / mNP-OPDL mix the thermomechanical response of the actuation performance is the same. For exploring the corresponding magnetically triggered remote actuation capability the nanocomposite with an AU to GU ratio of 85/15 (wt/wt) and homogeneously dispersed mNP-OCL was selected.

Based on the inductive heating capacity induced by the AMF response of the mNP in the composite, (in detail described in SI 3.2 Magnetic Heating Behavior), the actuation magnetic field strength was set to $H_{\text{act}} = 11.2 \text{ kA} \cdot \text{m}^{-1}$. Here, the crystalline AUs were completely molten, while $H_{\text{reset}} = 30 \text{ kA} \cdot \text{m}^{-1}$ was utilized to achieve completely amorphous nanocomposites applied for programming and reprogramming of the actuators.

The schematic drawing in Figure 1 B illustrates the programming and actuation pathway of a nanocomposite actuator material along with related illustrations of the morphological changes (i.e. AU and GU). Here, programming by elongation enabled magnetic field induced reversible contraction and expansion upon switching between H_{act} and H_{off} . After erasing the stretched actuation geometry by application of H_{reset} , and subsequent reprogramming to a bent actuator type, reversible changes in the bending angle were achieved. The reprogrammability function of the actuators was demonstrated by realization of multiple remote-controlled actuation geometries for a single nanocomposite strip as shown in the image series in Figure 2 A. Here, the magnetically triggered reversible performance increases ($H_{\text{act}} = 11.2 \text{ kA} \cdot \text{m}^{-1}$) and decreases (H_{off}) the bending angle (θ). Subsequent reprogramming to a clip, which closes at H_{act} and opens at H_{off} , reprogrammed to a concertina reversibly expanding (H_{act}) and contracting (H_{off}), and finally reprogrammed to a ring device opening at H_{act} and closing at H_{off} is documented and analyzed as different possible demonstrator geometries.

For investigating the long-term actuation performance under stress-free conditions, a multicycle magnetic experiment comprising 600 H_{act}/H_{off} -cycles with an exposure time of 120 s was conducted with a bent shaped specimen, to monitor the reversible changes in the bending angle. The observed reversible changes in the average bending angles from $52.4\pm 0.9^\circ$ (H_{off}) to 68.4 ± 0.9 (H_{act}) with the number of cycles are shown in [Figure 2 B](#) and the respective [SI video S1](#). Statistical analysis revealed a very stable actuation performance average of $\Delta\theta = 15.7\pm 0.3^\circ$, while only a minor drift of 0.4° per 100 H_{act}/H_{off} -cycles was found in the first 150 cycles (see [SI section 4.2 Remote Actuation Behavior](#)). This initial drift might be related to a kind of vibration training for the geometry determining units. Whereby, especially small (low melting) OPDL crystallites are destroyed during the periodic thermomechanical oscillations until a long term stable skeleton arrangement is established in the actuating material after 150 repetitive thermocycles.

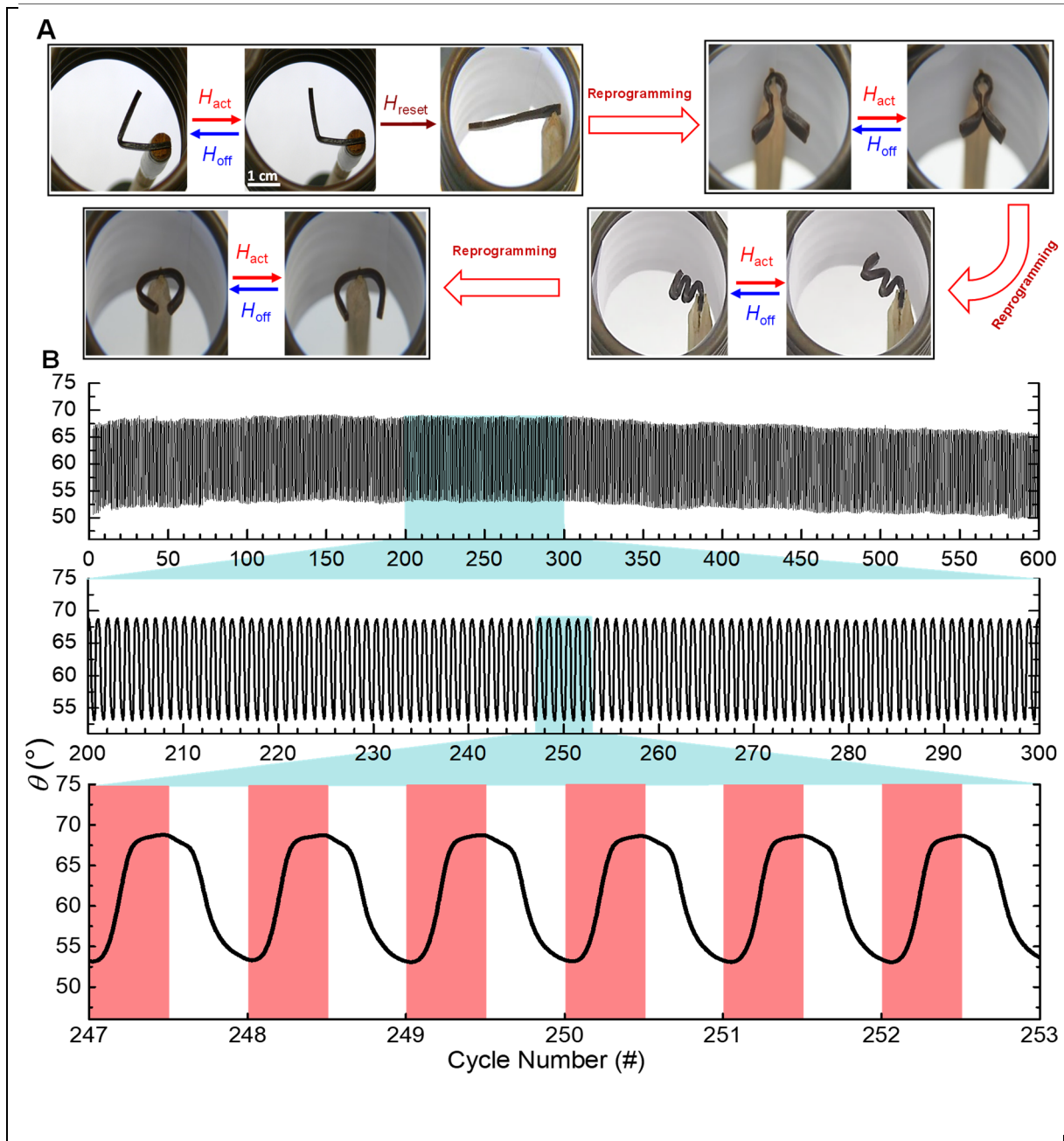


Figure 2: A) Image series demonstrating the reprogrammability of one and the same sample to different actuation geometries as well as the magnetically triggered reversible shape changes when switching between $H_{\text{act}} = 11.2 \text{ kA}\cdot\text{m}^{-1}$ and H_{off} : (i) decreasing and increasing bending angle, (ii) opening and closing of a clip, (iii) contraction and expansion of a concertina, and (iv) closing and opening of a ring. B) Bending angle θ as function of cycle number obtained in a multi-cyclic experiment with 600 actuation cycles by switching the magnetic field strength between $H_{\text{act}} = 11.2 \text{ kA}\cdot\text{m}^{-1}$ and $H_{\text{off}} = 0 \text{ kA}\cdot\text{m}^{-1}$.

In a next step, the influence of applying different magnetic field strengths and the variation of the exposure time on the remote actuation behavior were investigated as suitable control parameters for tuning the actuation performance. As the achievable temperature in the

nanocomposites increases with increasing H , the first experiment aimed at identifying the H interval where the AUs are molten partially or completely, while the GUs stay in the crystalline state. Here, $H_{\text{act}}/H_{\text{off}}$ experiments were conducted at different distinct H values in the range of 0 to 30 $\text{kA}\cdot\text{m}^{-1}$ resulting in changes in the bending angle $\Delta\theta = \theta_A - \theta_B$. The obtained dependence of $\Delta\theta$ on the applied H is shown in [Figure 3 A](#). To enable any reversible actuation a minimum value of $H_{\text{act}} = 7 \text{ kA}\cdot\text{m}^{-1}$ was required. The maximum $\Delta\theta = 20\pm 3^\circ$ was observed at $H_{\text{high}} = 11.2 \text{ kA}\cdot\text{m}^{-1}$. Further increase of H caused a decrease in $\Delta\theta$ until the irreversible change in bending angle was observed at $H_{\text{reset}} = 30.0 \text{ kA}\cdot\text{m}^{-1}$. Based on these results we selected three H values for more detailed investigations: $H_{\text{low}} = 10 \text{ kA}\cdot\text{m}^{-1}$ to $H_{\text{mid}} = 10.5 \text{ kA}\cdot\text{m}^{-1}$ and finally to $H_{\text{high}} = 11.2 \text{ kA}\cdot\text{m}^{-1}$. By decreasing H from H_{high} to H_{mid} , and H_{low} significant decreases in both recovery angles θ_A ($70\pm 1^\circ$ to $60\pm 1^\circ$ and $53\pm 1^\circ$; data from 2nd cycle) and θ_B ($53\pm 1^\circ$ to $49\pm 1^\circ$ and $46\pm 1^\circ$; data from 2nd cycle) were observed in cyclic $H_{\text{act}}/H_{\text{off}}$ experiments with an exposure time of 120 s ([Figure 3 B](#)). Both, the increase in actuation performance ($\Delta\theta$) and maximum bending angle θ_A with raising H values are related to increasing amounts of AU melting at H_{act} and crystallizing at H_{off} . Along with the control of actuation performance ($\Delta\theta$), the rate of change of angle $\Delta\theta/\Delta t$ could also be influenced by application of different H . Generally, we observed a decrease in value of $\Delta\theta/\Delta t$ by lowering the applied H . During actuation, the $\Delta\theta/\Delta t$ resulted in an average value of $11.2\pm 1^\circ\cdot\text{min}^{-1}$ at H_{high} , which was decreased to $3.4\pm 1^\circ\cdot\text{min}^{-1}$ at H_{low} . The high actuation speed could be attributed to a higher heating rate at H_{high} compared to H_{low} . A similar change in $\Delta\theta/\Delta t$ during recovery was also observed and the $\Delta\theta/\Delta t$ value of $-9.2\pm 1^\circ\cdot\text{min}^{-1}$ at H_{high} was decreased to $-4.4\pm 0.2^\circ\cdot\text{min}^{-1}$ at H_{low} ([data are summarized in SI Table S6](#)).

Inductive heating experiments revealed increasing achievable temperatures when raising the magnetic field strength from H_{low} to H_{high} , which is caused by the increase in the effective heat generation constant \bar{P} from $0.315\pm 0.004 \text{ K}\cdot\text{s}^{-1}$ to $1.930\pm 0.015 \text{ K}\cdot\text{s}^{-1}$ ([see SI 3. Analysis of Magnetic Heating Function](#)). At $H_{\text{high}} = 11.2 \text{ kA}\cdot\text{m}^{-1}$, the melting temperature of the AU domains is reached approx. 50 s after H was switched on (see [Figure 3 C](#)). Isothermal melting

experiments for PCL at $T \sim T_m$ have shown melting periods below 30 s³³ so in the magnetic heating experiment, the AU melting related shape change in the nanocomposite might be completed within 40 to 80 s after H was switched on. The reverse motion related to the crystallization of AUs is initiated almost instantaneously after the magnetic field is switched off. Here, an exponential decay of T_{bulk} in the nanocomposite was observed until ambient temperature was reached within 100 to 200 s (see Figure 3 D). For PCL, the reported crystallization half time decreases exponentially from 10⁵ s at about 50 °C to about 10¹ s at 30 °C³⁴ (see SI 3.3 Cooling Behavior after Removing Magnetic Field). This results in a final crystallinity of $DOC_{\text{m,OCL}} \sim 30\%$ at 30 °C after 70 to 80 s. Therefore, it can be estimated that the crystallization related actuation might be completed in a time interval from 30 to 80 s after H was switched off.

The actuation kinetics are another important application relevant characteristic of actuators. Here the programmed bent nanocomposite sample was directly exposed to H_{high} for different exposure time periods (t) to evaluate the kinetics of the actuation. Initially, $t = 100$ s was applied, which enabled a complete melting of the actuating domains as $\theta_A \sim 70 \pm 1^\circ$ and a constant $\Delta\theta \sim 20 \pm 3^\circ$ were observed for every cycle (total cycle (n) = 4). An actuation rate $\Delta\theta/\Delta t$ of $9.2 \pm 0.8^\circ \cdot \text{min}^{-1}$ and a recovery rate of $5.9 \pm 0.2^\circ \cdot \text{min}^{-1}$ were observed. In the next four cycles t was decreased to 50 s. The decrease in t resulted in just a partial recovery of the sample ($\theta_A = 63 \pm 1^\circ$) as the complete melting of the AU could not be achieved. Analogous to the previous experiment, a similar decrease in minimum bending angle θ_B in each cycle was observed. The corresponding θ_A decreased also from $70 \pm 1^\circ$ to $64 \pm 1^\circ$ and the decreasing trend in θ_A continued with increasing cycle number. Nevertheless, the $\Delta\theta$ of $6 \pm 2^\circ$ was constant in each cycle. Moreover, a lower actuation rate $\Delta\theta/\Delta t$ of $8.1 \pm 0.3^\circ \cdot \text{min}^{-1}$ and recovery rate of $3.8 \pm 0.5^\circ \cdot \text{min}^{-1}$ were recorded. The lower rates could be attributed to the partial melting and slow crystallization process of OCL based AU. However, after four cycles, t was again increased to 100 s restoring the original values of both angles and $\Delta\theta/\Delta t$. The changes in the angle at two different t are

displayed in Figure 3 E. The durability of the magnetic actuation could be demonstrated by long exposure time periods to H and H_{off} . In such an experiment, a $t = 10$ min for actuation and recovery steps was used (Figure 3 F). No significant changes in the values of resulting θ_A and θ_B were observed when the actuation at two different magnetic field strengths (H_{high} and H_{low}) was carried out. This indicates that the applied magnetic field can stabilize the actuator at certain positions (θ_A or θ_B) for longer times and that the magnitude of this reversible actuation ($\Delta\theta$) depends only on the applied H .

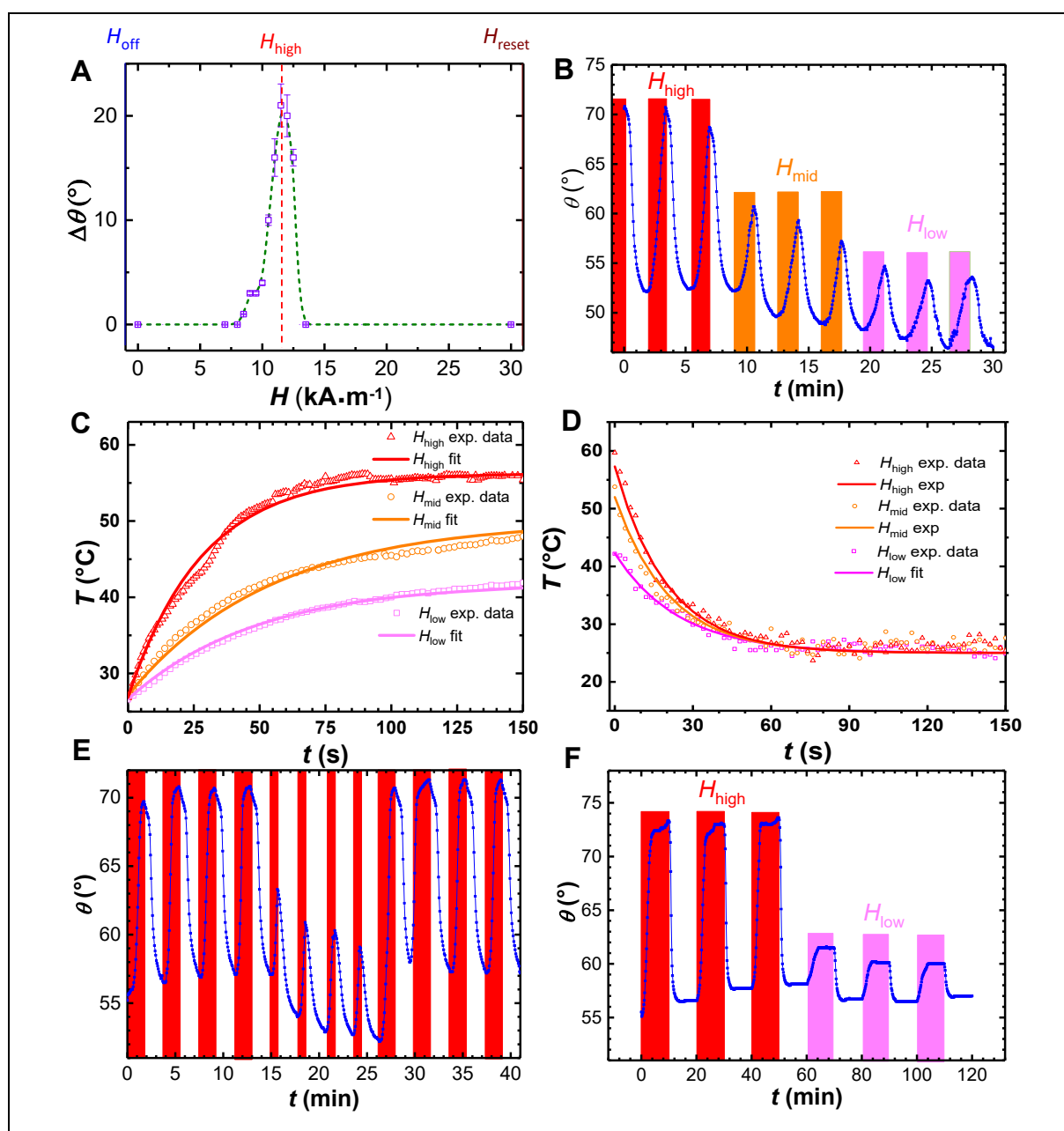


Figure 3: A) Dependence of magnetically-induced reversible change in the bending angle $\Delta\theta$ of a programmed nanocomposite specimen to the applied magnetic field strength H . B) Changes of the

bending angle (θ) by switching between H_{off} and $H_{\text{high}} = 11.2 \text{ kA}\cdot\text{m}^{-1}$ or $H_{\text{mid}} = 10.5 \text{ kA}\cdot\text{m}^{-1}$ or $H_{\text{low}} = 10.0 \text{ kA}\cdot\text{m}^{-1}$, during three cycles. C) Time dependent increase in surface temperature during magnetic heating experiments at H_{low} (magenta), H_{mid} (orange), H_{high} (red) and respective curve fittings (lines). D) Decrease in surface temperature after switching off H_{low} (magenta), H_{mid} (orange), H_{high} (red) and respective curve fittings (lines). E) Cyclic changes of the bending angle when sequentially exposed to various intervals of 100 s, 50 s, and 100 s to H_{high} . F) Cyclic changes in bending angle observed by switching between H_{high} or H_{low} and H_{off} using $t_{\text{exp}} = 10 \text{ min}$ in each step.

Finally, the applicability of this system was shown for a programmed multi-ring demonstrator, which could act as a gripper to grab or release objects. Exposure of the device to $H_{\text{high}} = 11.2 \text{ kA}\cdot\text{m}^{-1}$ caused a simultaneous partial opening of all three rings within 120 s, while switching to H_{off} resulted in the closure of all rings to the initial state of the device. The repetitive opening and closing of the demonstrator is shown in [SI video S2](#) and the observed change in distance (d) is presented in [SI Figure S11](#).

In conclusion, nanocomposite actuators capable of reprogrammable magnetically triggered motions have been realized. Different actuation geometries like a bending device, a length changing concertina, or a multi-ring opening device were demonstrated, whereby the actuation performance and actuation kinetics could be controlled by adequate selection of the applied magnetic field strength and the exposure time. The actuator showed long term durability by performing hundreds of free-standing reversible actuations upon repeated exposure to AMF. The original geometry of the actuator is reprogrammable and can be programmed to any new desired shape, which should enable the introduction of this material to a range of applications where different shapes are required to meet fast changing requirements. The melting and crystallization kinetics of the AUs limits the achievable actuation frequency. This limitation of the presented technology might be overcome by designing novel nanocomposite systems utilizing mNPs with exceptionally high intrinsic loss power³¹, fast crystallizing AUs like poly(ethylene)^{32, 35}, and additional cooling i.e. via a fan³⁶. It is anticipated that such remotely

addressable and reprogrammable actuators can act as key components in artificial muscles or soft robotics.

Author Contributions

AL, KK and MB designed the experiments. All authors participated (to different degrees) in interpreting the experimental results and writing the manuscript. LW, MYR, UN, YJ performed the experiments and analyzed the data.

Acknowledgements:

This work was supported by the Helmholtz-Association through programme-oriented funding. LW is grateful to China Scholarship Council (CSC) for a fellowship (grant No. 2010624124). The authors thank Ms. Susanne Schwanz, Ms. Yvonne Pieper as well as Ms. Nicole Schneider for technical support.

Conflicts of interest:

Authors state that they have no conflict of interest to declare.

Electronic Supplementary Information (ESI) available: Experimental details, tables, figures and two movies.

References

1. S. Bauer, S. Bauer-Gogonea, I. Graz, M. Kaltenbrunner, C. Keplinger and R. Schwödiauer, *Adv. Mater.*, 2014, **26**, 149-162.
2. A. D. Marchese, R. K. Katzschmann and D. Rus, *Soft Robotics*, 2015, **2**, 7-25.
3. S. M. Mirvakili and I. W. Hunter, *Adv. Mater.*, 2018, **30**, 1704407.
4. D. Rus and M. T. Tolley, *Nature*, 2015, **521**, 467-475.
5. L. Ionov, *Mater. Today*, 2014, **17**, 494-503.
6. L. Hines, K. Petersen, G. Z. Lum and M. Sitti, *Adv. Mater.*, 2017, **29**, 1603483.
7. F. D. Jochum and P. Theato, *Chem. Soc. Rev.*, 2013, **42**, 7468-7483.
8. F. Connolly, C. J. Walsh and K. Bertoldi, *Proc. Natl. Acad. Sci. U. S. A.*, 2017, **114**, 51-56.
9. O. Kim, T. J. Shin and M. J. Park, *Nat. Commun.*, 2013, **4**, 2208.
10. K. Uh, B. Yoon, C. W. Lee and J.-M. Kim, *ACS Appl. Mater. Interfaces*, 2016, **8**, 1289-1296.

11. S. Taccola, F. Greco, E. Sinibaldi, A. Mondini, B. Mazzolai and V. Mattoli, *Adv. Mater.*, 2015, **27**, 1668-1675.
12. C. S. Haines, M. D. Lima, N. Li, G. M. Spinks, J. Foroughi, J. D. W. Madden, S. H. Kim, S. Fang, M. Jung de Andrade, F. Göktepe, Ö. Göktepe, S. M. Mirvakili, S. Naficy, X. Lepró, J. Oh, M. E. Kozlov, S. J. Kim, X. Xu, B. J. Swedlove, G. G. Wallace and R. H. Baughman, *Science*, 2014, **343**, 868-872.
13. M. Behl, K. Kratz, J. Zotzmann, U. Nöchel and A. Lendlein, *Adv. Mater.*, 2013, **25**, 4466-4469.
14. M. Behl, K. Kratz, U. Noechel, T. Sauter and A. Lendlein, *Proc. Natl. Acad. Sci. U. S. A.*, 2013, **110**, 12555-12559.
15. T. Yoshino, M. Kondo, J.-i. Mamiya, M. Kinoshita, Y. Yu and T. Ikeda, *Adv. Mater.*, 2010, **22**, 1361-1363.
16. L. Yang, K. Setyowati, A. Li, S. Gong and J. Chen, *Adv. Mater.*, 2008, **20**, 2271-2275.
17. Z. Li, Y. Yang, Z. Wang, X. Zhang, Q. Chen, X. Qian, N. Liu, Y. Wei and Y. Ji, *J. Mater. Chem. A*, 2017, **5**, 6740-6746.
18. M. A. Zainal, A. Ahmad and M. S. Mohamed Ali, *Biomed. Microdevices*, 2017, **19**, 8.
19. S. Muzalifah Mohd, Y. Jumril, B. Badariah, H. Azrul Azlan and M. Burhanuddin Yeop, *J. Micromech. Microeng.*, 2017, **27**, 075027.
20. H. Wei, Q. Zhang, Y. Yao, L. Liu, Y. Liu and J. Leng, *ACS Appl. Mater. Interfaces*, 2017, **9**, 876-883.
21. V. Q. Nguyen, A. S. Ahmed and R. V. Ramanujan, *Adv. Mater.*, 2012, **24**, 4041-4054.
22. R. M. Erb, J. J. Martin, R. Soheilian, C. Pan and J. R. Barber, *Adv. Funct. Mater.*, 2016, **26**, 3859-3880.
23. W. Hu, G. Z. Lum, M. Mastrangeli and M. Sitti, *Nature*, 2018, **554**, 81-85.
24. J. Kim, S. E. Chung, S. E. Choi, H. Lee, J. Kim and S. Kwon, *Nat. Mater.*, 2011, **10**, 747-752.
25. J. M. Haberl, A. Sánchez-Ferrer, A. M. Mihut, H. Dietsch, A. M. Hirt and R. Mezzenga, *Adv. Mater.*, 2013, **25**, 1787-1791.
26. B. Klockner, P. Daniel, M. Brehmer, W. Tremel and R. Zentel, *J. Mater. Chem. C*, 2017, **5**, 6688-6696.
27. A. Kaiser, M. Winkler, S. Krause, H. Finkelmann and A. M. Schmidt, *J. Mater. Chem.*, 2009, **19**, 538-543.
28. R. Mohr, K. Kratz, T. Weigel, M. Lucka-Gabor, M. Moneke and A. Lendlein, *Proc. Natl. Acad. Sci. U. S. A.*, 2006, **103**, 3540-3545.
29. F. H. Zhang, Z. C. Zhang, C. J. Luo, I. T. Lin, Y. Liu, J. Leng and S. K. Smoukov, *J. Mater. Chem. C*, 2015, **3**, 11290-11293.
30. M. Heuchel, M. Y. Razzaq, K. Kratz, M. Behl and A. Lendlein, *Polymer*, 2015, **65**, 215-222.
31. J.-t. Jang, J. Lee, J. Seon, E. Ju, M. Kim, Y. I. Kim, M. G. Kim, Y. Takemura, A. S. Arbab, K. W. Kang, K. H. Park, S. H. Paek and S. Bae, *Adv. Mater.*, 2018, **30**, 1704362.
32. M. Farhan, T. Rudolph, U. Nöchel, W. Yan, K. Kratz and A. Lendlein, *ACS Appl. Mater. Interfaces*, 2017, **9**, 33559-33564.
33. T. Sasaki, *J. Therm. Anal. Calorim.*, 2013, **111**, 717-724.
34. S. Adamovsky and C. Schick, *Thermochim. Acta*, 2004, **415**, 1-7.
35. P. Supaphol and E. Spruiell Joseph, *J. Polym. Sci., Part B: Polym. Phys.*, 1998, **36**, 681-692.
36. M. Y. Razzaq, M. Behl, K. Kratz and A. Lendlein, *Adv. Mater.*, 2013, **25**, 5514-5518.